ChemComm

Mesoporous Perovskite Titanates via Hydrothermal Conversion

COMMUNICATION

Mesoporous Perovskite Titanates via Hydrothermal Conversion

Tianyu Li[a] and Efrain E. Rodriguez[a]

We demonstrate the successful hydrothermal conversion of mesoporous TiO₂ to mesoporous perovskite SrTiO₃. This method allows for control of pore size distribution and can be readily applied for the preparation of other mesoporous titanates such as BaTiO₃ and Li₂TiO₃. Such high-surface perovskites have potential in high-temperature applications due to their thermal stability.

ABO_3 perovskite oxides have drawn great interest in multiple research fields such as catalysis[1,2], solid oxide fuel cells[3] and oxygen storage[4] due to their highly modifiable structure, adjustable chemical composition, and extraordinary thermal and mechanical stabilities. $SrTiO_3$ is one of the most studied perovskite oxides and is widely used as a photocatalyst and support for other catalysts[5,6]. Compared with the various polymorphs of TiO_2, $SrTiO_3$ is chemically more modifiable (i.e., can support more doping and substitutions) and displays superior thermal and mechanical stabilities. However, high surface areas (100-300 m²/g) are easily achievable in mesoporous TiO_2 whereas most reports for $SrTiO_3$ show low surface areas (<10m²/g). The low surface area of $SrTiO_3$ materials greatly limits potential applications in catalysis.

Great effort has been made to synthesize mesoporous metal oxides for various applications[7–9]. To synthesize a mesoporous oxide, one usually employs templates (including silicates[10,11] carbon[12], and block copolymers[13–15]) to control the final pore architecture. The main impediment for preparing mesoporous $SrTiO_3$ with high surface areas lies in the relatively high preparation temperatures compared to those of binary metal oxides. Since the synthetic temperature of TiO_2 is relatively low (< 400°C), such templates persist during synthesis or break down slowly enough to preserve the porosity[16]. Common approaches to synthesize $SrTiO_3$ include either solid state[17] or sol-gel reactions[18]. Both reactions occur at relatively high

temperatures (> 700°C) and are therefore not amenable to traditional templating strategies. Soft templates will break down before ternary oxides such as $SrTiO_3$ can crystallize. Hard templates, such as carbon or silica, either react with $SrTiO_3$ or the precursors and are not suitable for obtaining pure products. To circumvent the problem of thermal instability of templating agents, we must turn down the temperature of synthesis. We found a reaction that occurs at significantly lower temperatures to form $SrTiO_3$. $SrTiO_3$ can form at 100-300°C through a hydrothermal reaction between solid TiO_2 and $Sr(OH)_2$ solutions[19,20]: $TiO_2(s) + Sr(OH)_2(aq) \rightarrow SrTiO_3(s) + H_2O(l)$. As mentioned previously, mesoporous TiO_2 can be easily prepared via plenty of routes. Thus, our strategy is to convert mesoporous TiO_2 into mesoporous $SrTiO_3$ via this hydrothermal reaction instead of directly synthesis of mesoporous $SrTiO_3$ through precursor reagents on a template. This alternative approach should be more facile due to the significantly lower reaction temperatures. In this study, we explore hydrothermal reactions between solid TiO_2 and $Sr(OH)_2$ solutions and study the best routes for the conversion of mesoporous TiO_2 to mesoporous $SrTiO_3$. We summarize our three major strategies and findings in the schematic presentation shown in **Figure 1**.

First, we present direct conversion of mesoporous crystalline TiO_2 to $SrTiO_3$ under hydrothermal conditions. We synthesized high surface area mesoporous crystalline TiO_2 *via* the Evaporation Induced Self-Assembly (EISA) method reported elsewhere[16]. Next, we placed the as-synthesized mesoporous crystalline TiO_2 in water with excessive $Sr(OH)_2$, followed by hydrothermal treatment at 200°C for 24 hours. The solid product was washed several times with dilute acetic acid and water to remove excess $Sr(OH)_2$ and then dried in air at 90 °C. The detailed synthesis, as well as the basic characterizations, are presented in the supplementary information (SI) file. The X-ray diffraction (XRD) powder pattern (**Figure 1c**) reveals a pure cubic phase of $SrTiO_3$, indicating a full conversion of mesoporous crystalline TiO_2 into $SrTiO_3$. However, from Transmission Electron Microscopy (TEM) **(Figure 1b)**, we observed that the original porosity of mesoporous crystalline

a. a Department of Chemistry and Biochemistry, University of Maryland, College Park, Maryland 20742-2115, USA
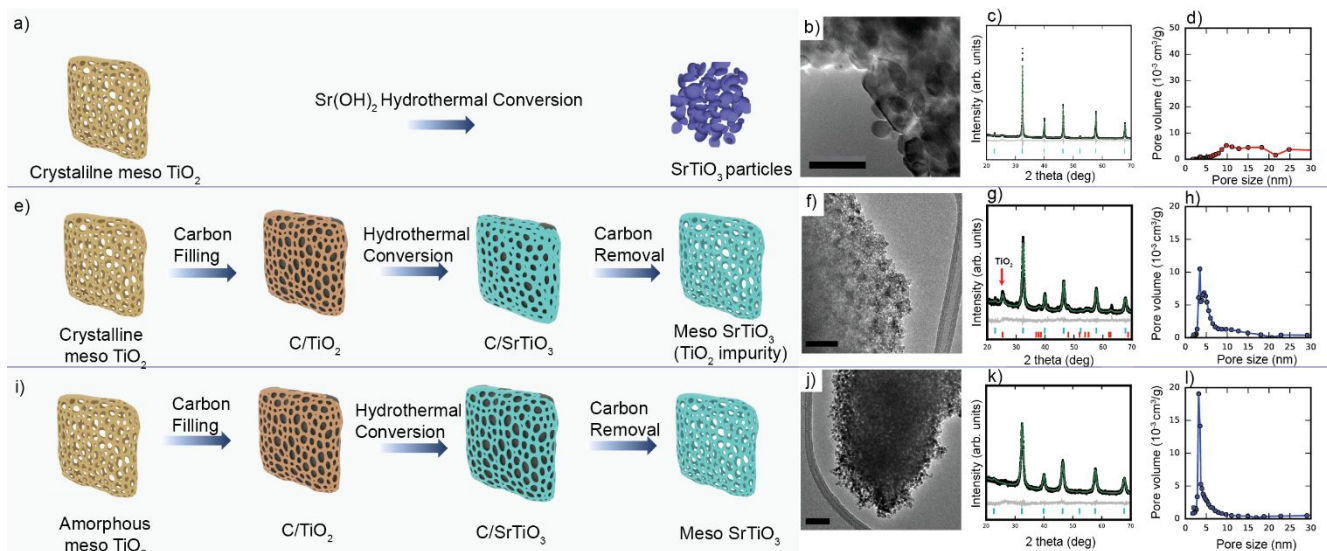
Figure 1. Illustration of strategies as well as TEM, XRD and pore distribution (From nitrogen adsorption measurement) results for converting mesoporous TiO_2 into mesoporous $SrTiO_3$: a)-d) Direct hydrothermal conversion. e)-h) Hydrothermal conversion of mesoporous crystalline TiO_2 after filling carbon support into pores. i)-l) Hydrothermal conversion of amorphous TiO_2 after filling carbon support into pores. Scale bar of the TEM is 100 nm.

TiO_2 was totally lost after the direct conversion to $SrTiO_3$. The TEM image clearly shows that $SrTiO_3$ products are nanoparticles with the size range of 30-50 nm, much larger than the single grain size of original mesoporous TiO_2 (~10 nm). Rietveld refinement of the crystal structure with the XRD powder pattern indicates the refined crystalline size of $SrTiO_3$ is ~50 nm, consistent with TEM observation. The surface area and pore volume of the original mesoporous TiO_2 is 205.7 m^2/g and 0.345 cm^3/g, respectively; they dramatically decrease to 15 m^2/g and 0.05 cm^3/g after conversion. Therefore, while this route affords full conversion of TiO_2 to $SrTiO_3$, the change only occurred at the atomic scale while the microstructure was completely lost.

The hydrothermal conversion of TiO_2 into $SrTiO_3$ in $Sr(OH)_2$ is reported to be a dissolution–precipitation process[20] whereby TiO_2 first dissolves in the highly basic solution and then recrystallizes to $SrTiO_3$. In mesoporous TiO_2, the closely packed particle grains help form the porous structure. The dissolution–precipitation process will therefore destroy the original porous structures, which cannot be recovered when $SrTiO_3$ precipitates due to the lack of any structure directing agent during the recrystallization step. Converting mesoporous TiO_2 to $SrTO_3$ while retaining porosity is not likely with only $Sr(OH)_2$ as the mineralizer. We therefore investigated alternative routes.

Since random and unconfined recrystallization of $SrTiO_3$ during the hydrothermal treatment prevents direct conversion, our next step was to effectively confine recrystallization during the hydrothermal treatment of mesoporous TiO_2. A common strategy to limit recrystallization is to use a physical barrier (template or support). Thus, we decided to fill the pores of mesoporous crystalline TiO_2 with a support before hydrothermal treatment. We started from the same mesoporous crystalline TiO_2 and then filled its pores with sugar (glucose). We then calcinated the mixture under Ar to carbonize the sugar. Once the composite TiO_2/carbon was formed, we treated it hydrothermally using

the same treatment previously described. We recovered the final product after calcination in air at 450 °C for 4h to fully burn out the carbon support.

From this second procedure, we clearly see a mesoporous structure retained after hydrothermal treatment, as shown in the TEM images of the final product (**Figure 1f**). The particles, stacked to form the mesopores, are around 16.6 nm in size, which indicates that the carbon support during the hydrothermal conversion effectively confines $SrTiO_3$ recrystallization. The BET surface area of the product is 58 m^2/g, far beyond the previous $SrTiO_3$ product from the direct hydrothermal conversion. **Figure 1h** displays the pore distribution from nitrogen adsorption isotherms. The narrow pore size distribution indicates the mesoporous nature of the material is maintained. We found the mean pore size to be around 4 nm, smaller than the mean pore size of the original TiO_2 material (6nm). The pore volume is smaller (0.078 cm^3/g) than the original TiO_2 (0.345 cm^3/g), and we attribute the decrease of the pore size and volume to lattice expansion from anatase TiO_2 to perovskite $SrTiO_3$.

While the carbon support maintains the porous structure during hydrothermal conversion, unreacted TiO_2 remained in the final product. Selected Area Electron Diffraction (SEAD) images (**Figure S2f**) shows diffraction peaks from anatase TiO_2 in addition to cubic $SrTiO_3$. Diffraction peaks from anatase are also present in the XRD powder patterns, and structural refinements (**Figure 1g**) indicate around 24 wt. % anatase in the final product. Even after increasing the hydrothermal reaction time from 24 h to 96 h, we still observed around 10 wt. % anatase TiO_2 (**Figure S5**) in the final product. A clue as to the incomplete conversion from TiO_2 to $SrTiO_3$ comes from surface area measurements: while the original mesoporous TiO_2 has a surface area of around 200 m^2/g, after filling with the carbon support, it falls below 5 m^2/g. We believe the lower surface area from the filled pores leads to slower reaction kinetics.

Using a carbon support proved to be an effective approach to maintaining porosity but resulted in slow reaction kinetics. We therefore strategized to use amorphous instead of crystalline TiO_2 since amorphous materials can display higher reactivities and smaller lattice energies. We synthesized mesoporous amorphous TiO_2 via a modified EISA method[21]. Weak diffraction peaks observed in the XRD pattern (**Figure S6a**) confirms its amorphous nature. Nitrogen adsorption measurements show it has a similar surface area and pore size distribution as the mesoporous crystalline TiO_2 (**Figure S7**). We then adapted the same procedure to fill the carbon support, conducted hydrothermal conversion for 24h and finally removed the carbon support to yield mesoporous $SrTiO_3$.

Through various characterization techniques, we found that this new procedure produced pure and mesoporous $SrTiO_3$ product (**Figure 1i-l**). TEM images and nitrogen adsorption measurements confirm that the $SrTiO_3$ from mesoporous amorphous TiO_2 retains its mesoporous nature. We detected no anatase TiO_2 phase from both SEAD and XRD. The HRTEM image is shown on **Figure S8c.** We mostly observe lattices from the (110) and (001) facets, which are commonly exposed in $SrTiO_3$ nanomaterials. Given that amorphous materials do not display sharp diffraction peaks, it is possible that some residual amorphous TiO_2 remains in final mesoporous $SrTiO_3$. To verify there is no amorphous TiO_2 left in the product, we calcined both mesoporous amorphous TiO_2 and our mesoporous $SrTiO_3$ in air. After calcination in air at 450 °C for 4 h, XRD (**Figure S9b)** shows that the amorphous TiO_2 crystalized to the anatase phase. However, for the mesoporous $SrTiO_3$ product, no other crystalline phase appeared even after 8h of calcination at 650°C in air **(Figure S10**). Therefore, TiO_2 fully converted to $SrTiO_3$ after hydrothermal treatment. We note that the surface area and refined crystal grain size (**Figure S10**) of the mesoporous $SrTiO_3$ remained nearly identical after the calcination step.

Our final strategy of using a carbon support and starting with amorphous TiO_2 was successful but still involved multiple reaction steps. We therefore considered ways to simplify the syntheses. It has been reported that carbon-filled TiO_2 composites can be directly synthesized by adding a carbon source during the EISA process[22]. Using a similar strategy (adding a certain amount of sugar in the EISA process), we directly synthesized amorphous TiO_2/C composites and treated them hydrothermally with $Sr(OH)_2$. This simplified procedure worked well enough to produce mesoporous $SrTiO_3$ with relatively high surface areas. However, TEM and nitrogen adsorption **(Figure S11)** measurements indicate that the TiO_2/C composites were still porous, though much less than the mesoporous TiO_2. By reintroducing the step of filling with a carbon support during the whole process, we observed a larger surface area (74 vs 54 m^2/g) and a more confined pore size distribution (**Figure S12**). Thus, filling carbon into mesoporous TiO_2 worked better than preparing and using TiO_2/C as the precursor to $SrTiO_3$.

Interestingly, the pore sizes of $SrTiO_3$ from the TiO_2/C composites are much larger than the ones from carbon-filled TiO_2 (12 vs. 4 nm), as presented in **Figure S15**. Such observation indicates one can control the pore size distribution of

mesoporous $SrTiO_3$ using the TiO_2/C composite as a precursor. Based on this hypothesis, we synthesized several TiO_2/C composites by varying the ratios of the carbon source (sugar) to Ti-precursor during the EISA. We also filled the composites with an extra carbon support to maximize confinement during the hydrothermal conversion. As presented in **Figure 2b**, the pore size of $SrTiO_3$ can be effectively adjusted from 4 nm to 12 nm by adding a different amount of carbon source during the EISA step. By increasing the carbon ratio in the TiO_2/C composites, the gaps between TiO_2 grains grow, which leaves larger pore after removing the carbon. Besides pore size enlargement, we also found the pore size distribution becomes wider as the carbon ratio is increased, which is possible because adding sugar disrupts the EISA process.

Small Angle X-ray Scattering (SAXS) (**Figure 2c**) on all samples is free of Bragg peaks, indicating that the mesopores are disordered. The small signature around q = 10^{-3} Å correlate to the mesopores, and moves linearly towards lower q (i.e., to larger size in real space) as the carbon(sugar) ratio was increased during synthesis. This observation in the SAXS data is consistent with the pore size distribution from nitrogen adsorption measurements. In the Porod region (high q-range) of the SAXS data, all scattering curves show log I independence of log q^4, implying the stacking grains are nearly spherical[23]. The scattering data is therefore consistent with the observed shapes of particle grains in the TEM images **(Figure S4 and S14)**. The surface areas of mesoporous $SrTiO_3$ are listed in **Table S3**, and those of some representative $SrTiO_3$ materials are listed in **Table S5** for comparison. The largest surface areas among our
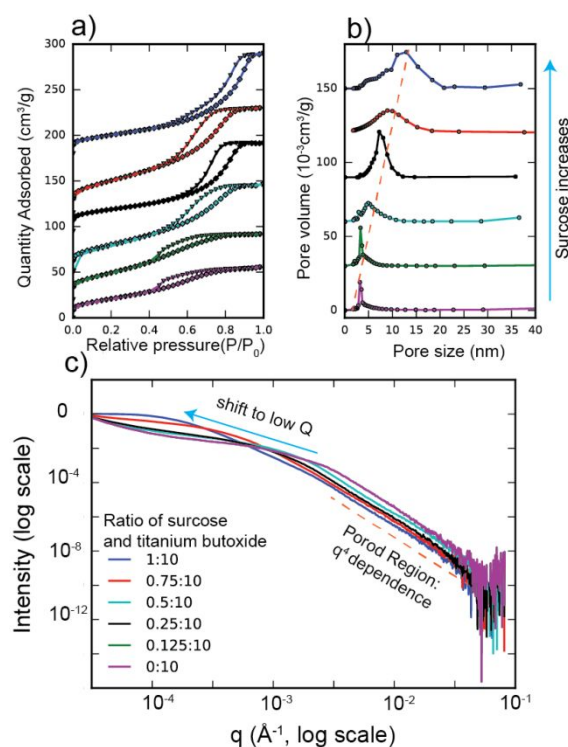
Figure 2. a) Nitrogen adsorption/desorption isotherm, b) Pore size distribution and c) Small Angle X-ray Scattering characterization of mesoporous $SrTiO_3$ from hydrothermal conversion of TiO_2/C composite with different carbon (sucrose) ratio.

samples reach up to 127m^2/g, which is among one of the highest reported on mesoporous SrTiO$_3$. While the surface area of mesoporous SrTiO$_3$ is lower than that of the original TiO$_2$ (~200m^2/g), SrTiO$_3$ is much heavier than TiO$_2$. If we convert the unit of surface area from m^2/g to m^2/mol, the surface area of as-synthesized SrTiO$_3$ (23446 m^2/mol) is higher than that of mesoporous TiO$_2$ (16008 m^2/mol), as shown in **Table S3**.

Up to now, we have demonstrated that we can convert mesoporous TiO$_2$ to mesoporous SrTiO$_3$ with tunable pore size distributions. We wanted to know, however, whether our synthesis is more general than that of preparing SrTiO$_3$. We therefore applied it towards the preparation of other ternary titanates. BaTiO$_3$ and CaTiO$_3$ are also perovskite oxides with wide applications. By simply switching Ba(OH)$_2$ from Sr(OH)$_2$ in the hydrothermal treatment, mesoporous BaTiO$_3$ with tunable pores can be synthesized **(Figure S16 and S17)**. The surface area of our mesoporous BaTiO$_3$ is already one of the highest among the reported BaTiO$_3$ materials. However, we could not prepare mesoporous CaTiO$_3$ with our method, likely because of the low solubility of Ca(OH)$_2$. Mesoporous Li$_2$TiO$_3$ with narrow pore size distribution can be also synthesized by switching to LiOH from Sr(OH)$_2$ (Figure **S18**). Li$_2$TiO$_3$ is an anode material in the fast-charging lithium battery systems, so the utilization of mesoporous Li$_2$TiO$_3$ could maximize the contact between electrode and electrolyte to further promote the kinetics of electrochemical processes.

In summary, we successfully synthesized mesoporous SrTiO$_3$ via hydrothermal conversion of mesoporous TiO$_2$. We found two key steps for successful conversion: 1) utilization of a carbon support to retain porosity during the hydrothermal treatment, and 2) utilization of amorphous instead of crystalline TiO$_2$ to speed up reaction kinetics. The as-synthesized mesoporous SrTiO$_3$ displays a narrow pore size distribution. This method allows us to control pore size by a simple adjustment of the carbon source ratio during the EISA synthesis of TiO$_2$. The tunability of the pore size distributions might broaden the applications of mesoporous SrTiO$_3$. Our method can also be easily modified to synthesize mesoporous BaTiO$_3$ and Li$_2$TiO$_3$ with high surface areas. Our method does not require high precision of reaction parameters to control the synthesis and can be easily scaled up. Mesoporosity in perovskites can lead to improvement in their electro- or photocatalytic activities as larger surface areas allow for more efficient electron/photon collection and contact with reactants. Furthermore, with much higher surface areas, these oxides now can host active metal clusters or even single atoms at concentrations sufficiently high to boost catalytic activity[24]. Compared with most mesoporous binary metal oxides, mesoporous perovskite SrTiO$_3$ and BaTiO$_3$ possess outstanding thermal and mechanical stability, implying their potential in high temperature settings.

Conflicts of interest

The authors declare no competing financial interest.

References

1   J. Zhu, H. Li, L. Zhong, P. Xiao, X. Xu, X. Yang, Z. Zhao and J. Li, *ACS Catal.*, 2014, **4**, 2917–2940.

2   M. A. Peña and J. L. G. Fierro, *Chem. Rev.*, 2001, **101**, 1981–2017.

3   S. J. Skinner, *Int. J. Inorg. Mater.*, 2001, **3**, 113–121.

4   J. Vieten, B. Bulfin, F. Call, M. Lange, M. Schmücker, A. Francke, M. Roeb and C. Sattler, *J. Mater. Chem. A*, 2016, **4**, 13652–13659.

5   T. Takata, J. Jiang, Y. Sakata, M. Nakabayashi, N. Shibata, V. Nandal, K. Seki, T. Hisatomi and K. Domen, *Nature*, 2020, **581**, 411–414.

6   S. Ouyang, H. Tong, N. Umezawa, J. Cao, P. Li, Y. Bi, Y. Zhang and J. Ye, *J. Am. Chem. Soc.*, 2012, **134**, 1974–1977.

7   D. Gu and F. Schüth, *Chem. Soc. Rev.*, 2014, **43**, 313–344.

8   Y. Ren, Z. Ma and P. G. Bruce, *Chem. Soc. Rev.*, 2012, **41**, 4909–4927.

9   C. Li, Q. Li, Y. V. Kaneti, D. Hou, Y. Yamauchi and Y. Mai, *Chem. Soc. Rev.*, 2020, **49**, 4681–4736.

10 S. C. Laha and R. Ryoo, *Chem. Commun.*, 2003, **3**, 2138–2139.

11 X. Deng, K. Chen and H. Tüysüz, *Chem. Mater.*, 2017, **29**, 40–52.

12 X. Lai, X. Li, W. Geng, J. Tu, J. Li and S. Qiu, *Angew. Chemie - Int. Ed.*, 2007, **46**, 738–741.

13 P. Mei, Y. V. Kaneti, M. Pramanik, T. Takei, Ö. Dag, Y. Sugahara and Y. Yamauchi, *Nano Energy*, 2018, **52**, 336–344.

14 L. Liu, X. Yang, Y. Xie, H. Liu, X. Zhou, X. Xiao, Y. Ren, Z. Ma, X. Cheng, Y. Deng and D. Zhao, *Adv. Mater.*, 2020, **32**, 1906653.

15 D. Zhao, J. Feng, Q. Huo, N. Melosh, G. H. Fredrickson, B. F. Chmelka and G. D. Stucky, *Science (80-.).*, 1998, **279**, 548–552.

16 W. Li, Z. Wu, J. Wang, A. A. Elzatahry and D. Zhao, *Chem. Mater.*, 2014, **26**, 287–298.

17 Y. Liu, L. Xie, Y. Li, R. Yang, J. Qu, Y. Li and X. Li, *J. Power Sources*, 2008, **183**, 701–707.

18 W. Xuewen, Z. Zhiyong and Z. Shuixian, *Mater. Sci. Eng. B Solid-State Mater. Adv. Technol.*, 2001, **86**, 29–33.

19 F. A. Rabuffetti, H. S. Kim, J. A. Enterkin, Y. Wang, C. H. Lanier, L. D. Marks, K. R. Poeppelmeier and P. C. Stair, *Chem. Mater.*, 2008, **20**, 5628–5635.

20 V. Kalyani, B. S. Vasile, A. Ianculescu, A. Testino, A. Carino, M. T. Buscaglia, V. Buscaglia and P. Nanni, *Cryst. Growth Des.*, 2015, **15**, 5712–5725.

21 L. Robben, A. A. Ismail, S. J. Lohmeier, A. Feldhoff, D. W. Bahnemann and J. C. Buhl, *Chem. Mater.*, 2012, **24**, 1268–1275.

22 R. Liu, Y. Ren, Y. Shi, F. Zhang, L. Zhang, B. Tu and D. Zhao, *Chem. Mater.*, 2008, **20**, 1140–1145.

23 S. Ciccariello, *Acta Crystallogr. Sect. A*, 1989, **45**, 86–99.

24 S. Tanaka, J. Lin, Y. V. Kaneti, S. Yusa, Y. Jikihara, T. Nakayama, M. B. Zakaria, A. A. Alshehri, J. You, M. S. A. Hossain and Y. Yamauchi, *Nanoscale*, 2018, **10**, 4779–4785.